

On the role of shock waves in galaxy cluster evolution

Vicent Quilis , José M^a. Ibáñez

and

Diego Sáez

Departament d'Astronomia i Astrofísica, Universitat de València, E-46100 Burjassot,

València, Spain

Received _____; accepted _____

ABSTRACT

Numerical simulations of galaxy clusters including two species – baryonic gas and dark matter particles – are presented. Cold Dark Matter spectrum, Gaussian statistics and flat universe are assumed. The dark matter component is evolved numerically by means of a standard *particle mesh* method. The evolution of the baryonic component has been studied numerically by using a multidimensional (3D) hydrodynamical code based on *modern high resolution shock capturing* techniques. These techniques are specially designed for treating accurately complex flows in which shocks appear and interact. With this picture, the role of shock waves in the formation and evolution of rich galaxy clusters is analyzed. Our results display two well differentiated morphologies of the shocked baryonic matter: filamentary at early epochs and quasi-spherical at low redshifts.

Subject headings: cosmology: theory—hydrodynamics—large-scale structure of the universe —methods:numerical—shock waves

1. Introduction

Galaxy clusters are the largest systems gravitationally bounded in the Universe. Their study has been a fashion topic in Cosmology since last years. Work on topics related with galaxy clusters is worthy to: i) understand the formation, evolution, dynamics and morphology of these systems, ii) learn on the physical processes involved in them, and iii) find out some information concerning with fundamental parameters in Cosmology as density parameter (Ω), Hubble's constant (H), and the spectrum of the primordial density field.

During last years technical improvements have produced huge quantity of data about galaxy clusters. Let us mention the new galaxy surveys (Guzzo 1996, and references therein) and the extensive observation in X-rays using satellites as ROSAT or ASCA. These huge volume of data strongly motivates a lot of theoretical work trying to explain the observational results.

From the theoretical point of view, numerical simulations are the best tools to understand physics involved in galaxy clusters. At the beginning, numerical simulations of galaxy clusters were performed using N-body techniques. Since then, they have been extensively used and have produced important results (see, e.g, Efstathiou et al. 1985, Bertschinger & Gelb 1991, Xu 1995). Next step in the full description of galaxy clusters was to introduce in the picture a baryonic component. The numerical methods developed in order to deal with baryonic matter were more sophisticated and expensive in computational resources. As a consequence, it was not possible to carry out numerical simulations with two species (dark matter and baryonic gas) until late eighties.

Cosmological hydrodynamic codes have been usually classified in two main categories: a) the so-called Lagrangian methods, like the *Smoothed Particles Hydrodynamics* (SPH) or ulterior extensions based on them, and b) Eulerian codes.

SPH methods were first proposed by Gingold & Monaghan (1977), and Lucy (1977). Among the best features of this technique, it should be pointed out its high resolution in dense regions. This property is directly derived from its Lagrangian character. The first implementations of SPH techniques had some weak points: i) The low density regions were badly described due to the Lagrangian character of the method. ii) Discontinuities and strong gradients were poorly solved and an important diffusion was introduced. iii) They were not conservative. Nevertheless, these previous problems were overcome in the modern implementations of these techniques. Improved SPH techniques have been widely developed for cosmological applications (see, e.g., Evrard 1988, Hernquist & Katz 1989, Navarro & White 1993, Gnedin 1995).

Numerical cosmological codes using an Eulerian approach to study baryonic gas inside galaxy clusters have been also developed. Some of these hydro-codes use *artificial viscosity* in order to deal with shock waves (Cen 1992, Anninos et al. 1994). These techniques require a good calibration of the free parameters which are introduced by hand and state some numerical problems. Recently, a new family of finite difference methods, which use Eulerian approaches and avoid artificial viscosity, has been developed in numerical Cosmology. They are the so-called *high resolution shock capturing methods* (HRSC), the modern extensions of the original Godunov’s idea (1959). According to the Riemann solver and the procedure in order to achieve spatial accuracy, we can distinguish three groups: 1) the ones following Harten’s scheme (1983), like Ryu et al. (1993), 2) those using the analytical solution of the Riemann problem for the Newtonian dynamics of ideal gases and the PPM scheme described by Collela & Woodward (1984), like Bryan et al. (1994), and 3) the codes using Roe’s Riemann solver (Roe 1981) plus the MUSCL or PPM cell reconstruction, like in Quilis et al. (1996). In this last reference, the code used in present paper is described and tested appropriately.

An exhaustive comparison among all these kinds of cosmological hydrodynamic codes can be found in Kang et al. (1994).

Due to the Eulerian character of our code, it does not show –in dense regions– a resolution as good as the Lagrangian ones, and it requires more computational resources. However, HRSC schemes –by construction– have excellent properties in order to deal with shocks, discontinuities, and strong gradients. HRSC techniques typically solve shocks in two cells. Due to their intrinsic properties, the detection of shocks is independent on the number of cells used in the simulations. It should be pointed out that this last property is really important when three-dimensional simulations are carried out. In these simulations the size of the grid is a stringent constraint due to its high cost in computational resources. Moreover, these methods are conservative by construction, that is, quantities which should be physically conserved are numerically conserved up to the order of the method. It should be also noticed that these methods show good results in extreme low density regions (Einfeldt et al. 1991).

As it has been pointed out by several authors, the role of shock waves can be extremely important in order to understand the heating processes in the intracluster medium (ICM). In this paper we are interested in understanding and quantifying the role of shocks. In order to do that it is crucial to use numerical codes able to manage with complex flows. Yes, indeed, one of the important features of HRSC techniques is just to treat numerically shocks and strong discontinuities giving sharp profiles (in a few numerical cells, as we have mentioned above) independently of the size of the grid. Hence, formation, evolution, and interaction of shocks in 3D flows can be analyzed accurately with HRSC schemes, and, consequently, their use is absolutely justified in order to study shocks and their consequences on the ICM’s dynamics.

Hereafter, t stands for the cosmological time, t_0 is the age of the Universe, $a(t)$ is the

scale factor of a flat background. Function \dot{a}/a is denoted by H , where the dot stands for the derivative of a with respect to the cosmological time. Hubble constant is the present value of H ; its value in units of $100 \text{ Km s}^{-1} \text{ Mpc}^{-1}$ is the reduced Hubble constant h . In our computations we have assumed $h = 0.5$. Velocities are given in units of the speed of light. Baryonic, dark matter, and background mass density are denoted by ρ_b , ρ_{DM} , and ρ_B , respectively. The density contrast is $\delta_b = (\rho_b - \rho_B)/\rho_B$ for baryonic matter, analogously is defined δ_{DM} for dark matter.

The plan of this paper is as follows: In Section 2, our numerical cluster model is described. In Section 3, the results of the simulations are analyzed. Finally, a general discussion is presented in Section 4.

2. Cluster Model

2.1. Initial conditions

Initial conditions are given at redshift $z = 100$. We have considered a flat universe ($\Omega_o = 1$) and a CDM scenario. The density profile is obtained by using the power spectrum:

$$|\delta_k|^2 = \frac{\mathcal{A}k}{(1 + \beta k + \omega k^{\frac{3}{2}} + \gamma k^2)^2} \quad (1)$$

where $\beta = 1.7(\Omega_o h^2)^{-1} \text{ Mpc}$, $\omega = 9.0(\Omega_o h^2)^{-1.5} \text{ Mpc}^{1.5}$, $\gamma = (\Omega_o h^2)^{-2} \text{ Mpc}^2$, and the constant \mathcal{A} (normalization) has been fitted by using $\sigma_8 = 0.63$, where $\sigma_8 \equiv \langle (\frac{\delta\rho}{\rho})^2 \rangle^{\frac{1}{2}}$ on the $8 h^{-1} \text{ Mpc}$ scale. Assuming that the density field is Gaussian, realizations in the position space can be obtained from Eq.(1).

Hoffman and Ribak (1991) described a method to produce realizations of Gaussian fields under some constraints. This procedure was extended by van den Weygaert and Bertschinger (1996). We have used this powerful method in order to obtain the initial

conditions for our cluster. In particular, we have assumed three constraints: 1) the cluster peak is located just at the center of the box, its amplitude corresponds to the maximum density contrast in our initial box (64 Mpc per edge in comoving coordinates), 2) the mass enclosed inside a Gaussian ball, $M = (2\pi)^{(3/2)}\rho_B R_f^3$ with $R_f = 4h^{-1}$ comoving Mpc, is $M = 6 \times 10^{14} M_\odot$ –centered at the peak position–, and 3) the amplitude of the initial density contrast –cluster peak– is 3σ after smoothing on scales $\sim 4h^{-1}Mpc$ using a Gaussian window function.

The 3D Zeldovich’s approximation is used to evolve from the above initial conditions up to $z = 30$. At this redshift, a comoving box of 20 Mpc per edge is extracted (zoom) from the initial box. The maximum of the density contrast is located at the center of the new box.

The density and the velocity profiles of the initial perturbation are known after performing the zoom at $z = 30$. Then, we define the composition of this perturbation, namely, we fix the ratio between the dark matter (DM) and baryonic densities. It is considered that the 90 % of the matter is dark and the remaining is baryonic. The DM component is discretized into particles of the same mass (the mass of the particles depend upon the resolution of each simulation). The baryonic component is considered as an ideal fluid of adiabatic exponent γ , fully ionized, with mass abundances of 75% Hydrogen and 25% Helium, which represents the intracluster medium (ICM). We assume that the initial velocities of both components are identical. The initial homogeneous temperature is set up assuming that at $z = 30$ the temperature is given by $T_{30} = T_{200} \left(\frac{\rho_B(z = 30)}{\rho_B(z = 200)} \right)^{\gamma-1}$, where $T_{200} = 2.73(1 + z)$ with $z = 200$, and γ is the adiabatic exponent (see , e.g., Anninos & Norman 1996).

The above initial conditions give the seed for the formation of a large Abell cluster.

Some comments about the boundary conditions are deserved. The baryonic and DM

have low densities at the faces of the numerical box. Moreover, DM particles are not allowed to escape out the box. In order to do that, when one particle crosses some of the faces of the computational box, it is introduced through the symmetric face with the same velocity. Thus, a reasonable approximation to periodic boundary conditions is considered.

2.2. Nonlinear evolution

The nonlinear evolution of the baryonic component is described by the hydrodynamics equations (Peebles 1980):

$$\frac{\partial \delta_b}{\partial t} + \frac{1}{a} \nabla \cdot (1 + \delta_b) \vec{v} = 0 \quad (2)$$

$$\frac{\partial \vec{v}}{\partial t} + \frac{1}{a} (\vec{v} \cdot \nabla) \vec{v} + H \vec{v} = -\frac{1}{\rho_b a} \nabla p - \frac{1}{a} \nabla \phi \quad (3)$$

$$\frac{\partial E}{\partial t} + \frac{1}{a} \nabla \cdot [(E + p) \vec{v}] = -3H(E + p) - H \rho_b \vec{v}^2 - \frac{\rho_b \vec{v}}{a} \nabla \phi - \Lambda \quad (4)$$

and the evolution of the DM particles obeys the particle equations:

$$\frac{d\vec{x}}{dt} = \frac{\vec{v}}{a} \quad (5)$$

$$\frac{d\vec{v}}{dt} = -\frac{\nabla \phi}{a} - H \vec{v} \quad (6)$$

where \vec{x} , $\vec{v} = a(t) \frac{d\vec{x}}{dt} = (v_x, v_y, v_z)$, E and $\phi(t, \vec{x})$ are, respectively, the Eulerian coordinates, the peculiar velocity, the total energy $E = \rho_b \epsilon + \frac{1}{2} \rho_b v^2$ ($v^2 = v_x^2 + v_y^2 + v_z^2$), and the peculiar Newtonian gravitational potential. The pressure and the internal energy per unit mass are denoted, respectively, as p and ϵ . The above system of hydrodynamical equations is closed with the equation of state of an ideal gas $p = (\gamma - 1) \rho_b \epsilon$ and $\gamma = 5/3$ (monoatomic gas).

In some applications described in the present paper two cooling processes are taken into account, Compton cooling (Λ^C) and thermal Bremsstrahlung (Λ^{Br}). The well known expressions for these processes are (see, for instance, Umemura & Ikeuchi (1984)):

$$\Lambda^C = 5.4 \times 10^{-36} (1 + z)^4 n_e T \quad (\text{erg cm}^{-3} \text{s}^{-1}) \quad (7)$$

and

$$\Lambda^{Br} = 1.8 \times 10^{-27} n_e T^{\frac{1}{2}} (n_{HII} + 4n_{HeIII}) \quad (\text{erg cm}^{-3} \text{s}^{-1}) \quad (8)$$

where n_e , n_{HII} , and n_{HeIII} are the number density of electrons, protons, and helium nuclei, respectively. The cooling effects are introduced in the source term $\Lambda = \Lambda^C + \Lambda^{Br}$ in Eq.(4).

Both components, gas and particles, are gravitationally coupled through Poisson's equation:

$$\nabla^2 \phi = \frac{3}{2} H^2 a^2 \delta_T, \quad (9)$$

where $\delta_T = (\rho_b + \rho_{DM} - \rho_B)/\rho_B$ is the total density contrast.

The hydrodynamical equations (2-4) define a *hyperbolic system of conservations laws* (with sources). This important property allows us to apply a new powerful family of numerical methods (HRSC) in order to solve this system. The main features of these methods are summarized: 1) the quantities which should be physically conserved, are numerically conserved by construction, due to the fact that the algorithm is written in conservative form, 2) these methods are of high order in the smooth regions of the flow, 3) shocks are sharply solved in typically two numerical cells, independently of the number of cells used in the simulations, 4) numerical artifacts like *artificial viscosity* are avoided, 5) these methods are free of spurious oscillations around shocks, and 6) they are able to handle strong gradients and discontinuities. In Quilis et al. (1996) we took advantage of the hyperbolicity property of this system in order to design a multidimensional hydrodynamic code. A full description of this code and a set of tests proving its performance were presented in this reference. The above method is used in present paper in order to study the evolution of the baryonic gas.

The evolution of DM particles described by Eqs. (5-6) is studied through a standard Particle Mesh (PM) method (Hockney & Eastwood 1988). This method has some important features from the point of view of our applications: 1) the PM methods are widely extended

and well known, 2) they are easily programmable and can be directly coupled with a hydro-code, and 3) their CPU cost is quite low in comparison with others particle type methods. This last property is crucial when the particle code must be coupled with a hydro-code like the one described above where the computational effort is severe.

Poisson’s equation (9) is solved by using Fast Fourier Transform (FFT) methods (Press et al. 1987). In order to recover a continuous density contrast field for dark matter component, we use a standard cell-in-cloud (CIC) scheme (Hockney & Eastwood 1988) at each time step.

The time step is computed following Quilis et al. (1996). We have considered Courant’s and dynamical characteristic times. These times must be corrected in order to ensure the numerical stability of the algorithm. Typical values of these correction factors, known as CFL, are $CFL_{Courant} = 0.6$ and $CFL_{dynamical} \sim 10^{-2}$. Besides the characteristic times mentioned before, cooling processes introduce a new characteristic time. Nevertheless as it is known (Tsai et al. 1994), for the scales considered in this paper, the characteristic cooling time is larger than the dynamical one and, consequently, cooling would not expect to be an effective process.

In order to display the conservation properties of the whole code – hydro, particles and the Poisson solver – the global energy conservation is investigated in the Appendix A. Some comments on the numerical spatial resolution of our simulations are also discussed in Appendix B.

3. Results

In this Section we are going to discuss the results obtained running our code in two cases: i) *without cooling* processes (denoted by A), and ii) *including cooling* effects (denoted

by B).

Numerical simulations have been carried out using 128^3 DM particles and 128^3 baryonic cells. The physical comoving box size is 20 Mpc per edge. Since we are interested in the study of ICM and not concerned with smaller scales like galaxies themselves, the choice of 128^3 DM particles and 128^3 baryonic cells seems adequate. The resolution of the hydrodynamical code is ~ 0.15 comoving Mpc , however the PM code resolution is two cells. Hence, the minimal resolution of our simulations will be around ~ 0.3 comoving Mpc . Taking into account the properties of HRSC techniques, the grid used in present paper seems a reasonable compromise between the resolution needed in order to describe physical processes and our current computational limitations.

The CPU cost of our numerical simulations is 183.2 s (25.1 s) per time step (with 128^3 numerical cells, and 128^3 particles) in a Hewlett-Packard J280 (Silicon Graphics Origin 2000 with 8 processors for parallel version).

3.1. Cluster evolution

In the standard CDM scenario, clusters of galaxies grow by merging from smaller collapsed structures. This behaviour can be tested through N-body simulations. Figure 1 shows the DM particle distribution for our A simulation at six epochs. DM dynamics seems to be not much affected by gas dynamics and cooling effects. By this reason the results from B simulations are not shown. In Figure 1, 32^3 particles have been plotted. The edges of the boxes are 20 comoving Mpc length.

The implementation of a baryonic gas complicates the description of the cluster. This is a component with pressure and with a different dynamics. This new component could undergo compression, expansion, heating and cooling. Non-adiabatic processes

like shock waves and the cooling – due to Bremsstrahlung and Compton – could also be present. These deviations from adiabaticity are very important in order to understand the mechanism which provides an extra energy to ICM. Figure 2 shows ICM density contrast colour contours for A simulation. The slices are 20 (0.15) comoving Mpc length (depth). Four times are displayed. The evolutionary picture starts with collapsing processes of small substructures. These substructures undergo a merging process towards a well defined central object. This picture is valid for both simulations, A and B. Since no significant differences can be found, for the sake of brevity only A results have been displayed. These results supports the well known fact that for the scales considered in this paper, the cooling is not a relevant process (see ,e.g, Tsai et al. 1994).

A good description of the cluster evolution is given by the profiles, at different epochs, of the main quantities averaged in spherical shells. These shells are located at several radii from the cluster center. This center is defined as the minimum of the total gravitational potential. Each shell has a fixed comoving width. An average value inside the shell can be estimated for each variable. Figure 3 plots the average density contrast for baryonic gas (top panel) and DM (bottom panel) versus radial distance to the cluster center in comoving Mpc. In each panel several curves are shown corresponding to different times. As no significant differences arise between A and B simulations, only case A is presented. It should be pointed out the resemblance of the profiles plotted here and the ones shown by Navarro et al. (1995). As it was explained in detail in this reference, for the spatial resolution considered in this paper, both components evolve keeping the original ratios between their densities.

The gross properties of the cluster dynamics can be fairly inferred studying average radial velocities of DM and baryonic gas. These averages are computed in a similar way to the density contrast. Figure 4 plots the average radial velocities, in units of c , for baryonic

gas (top panel) and DM particles (bottom panel). As in Figure 3, only A results are shown.

From Figs. 3 and 4 the following stages in the evolution could be roughly distinguished. First, an infalling phase until $z \sim 2$, characterized by a typical profile in velocity (gas and DM) and increasing in density contrast (both components). Let us point out that the profile, during the infalling epoch, of the baryonic component remind us the typical one in any collapsing object, the minimum of which separates a subsonic homologously part (the inner one) from the supersonic freely falling part (the outer one). In a second phase, gas velocities change their signs in the inner part while outer shells go on falling. Gas density contrast slightly decreases due to the gas outflow. Nevertheless, this effect is subdominant, and the ratios between the averaged density profiles of gas and DM undergo small variations. DM particles are not affected by this dynamics and exhibit some tendency to reach a dynamical equilibrium.

3.2. Looking for shocks

In the present Section we are specially interested in giving a set of criteria allowing us to identify those regions where shocks form and evolve. In the next Section will analyze the energy released to the ICM by these shocks.

From the top panel of Figure 4 some strong evidences of the existence of a quasi-spherical shock are pointed out. The velocity profiles show how the evolution begins with a typical infalling profile. This velocity is strongly correlated with the growing of the baryonic density contrast, for the same time, in top panel of Figure 3. As the density rises, the pressure becomes more important. At $z \sim 2$, the velocities at the inner part of the cluster change their sign, and the gas moves out. This is an evidence of a quasi-spherical shock moving outwards from the core cluster.

Following Anninos and Norman (1996) we study the entropy $s = \ln(T/\rho_b^{\gamma-1})$. In an adiabatic process this quantity should keep constant. Variations in s are evidence of non-adiabatic processes. In particular shock waves strongly influence the variations in the entropy. The maximum in the entropy could identify the position of shocks. Figure 5 plots the average entropy in spherical shells for A case at several times.

The average entropy profiles evidence the existence of a quasi-spherical shock travelling outwards from the cluster center. The formation and evolution of the local maxima in the average entropy profiles can be directly correlated with the changes in the velocity profiles for baryonic gas (top panel Figure 4). The averaging procedure in shells is itself an important source of numerical diffusion. When the shock deviates from sphericity or there are a set of smaller and irregular shocks, then the average in spherical shells does not produce two regions separated by a sharp jump in the entropy profile. In Figure 5 two regions are clearly differentiated. The pre-shock region has a roughly constant entropy, while the post-shock shows a decreasing inward entropy with values higher than those of pre-shock region.

The above analysis evidences the existence of, at least, one quasi-spherical shock. Nevertheless, it is not possible to know if there is a unique quasi-spherical shock, or there are some shocks at several scales which in average give the global shock in Figure 5. From this Figure, no ideas about the scales and form of the shocks can be obtained. In order to clarify this point, Figure 6 shows slices for the divergence of baryonic velocity, entropy, temperature and pressure. These slices are centered at the point where the gas density is maximum, and are projected along z-axis. Size and depth of the slices are the usual through this paper (see Fig. 2).

As it has been mentioned above, entropy, pressure and temperature exhibit a well known behaviour in shocks. Nevertheless, some comments on the usefulness of studying

the divergence of baryonic velocity are worthwhile. If we assume that, at a given time, the density contrast δ_b is homogeneous, and that the source terms in Eq. (2) are negligible, then, the time variation of the density contrast is related with the divergence of the velocity through the following equation,

$$\frac{\partial \ln \delta_b}{\partial t} = -\frac{1}{a} \nabla \cdot \vec{v} \quad (10)$$

This equation points out two different regimes: 1) compression, i.e., $\nabla \cdot \vec{v} < 0$, and 2) rarefaction, i.e., $\nabla \cdot \vec{v} > 0$. Therefore, the changes in the sign of the divergence of the velocity allow us to distinguish between compressed and rarefied regions. This discussion can always be applied locally, and it gives a roughly description of the dynamical state of the system.

In our simulations, neighbouring regions might be separated by a shock if simultaneously, $\nabla \vec{v}$ exhibits large changes, the entropy increases clearly, and the temperature and pressure show strong gradients. The features of the slices for these quantities, allow us to have a good description of the shock scales and their morphology.

Strong evidences of a quasi-spherical shock travelling outwards appear in all the quantities plotted in Figure 6. A thin shell, where the divergence of baryonic velocity and temperatures change strongly and the entropy reaches their maxima values, is clearly appreciable. Pressure exhibits a tiny jump in the same region, but, unfortunately, due to the extreme variations in pressure from the center to the outer regions, the colour scale is not able to reproduce this pressure jump.

Even more, it is possible to define some criteria which could label a cell which is involved in a shock. Following the criteria used by Colella & Woodward (1984) to detect shocks, we generalize them for a multidimensional case. A numerical cell, (i, j, k) , is labelled

as involved within a shock if the following conditions are satisfied:

$$\frac{|p_{i+l,j+m,k+n} - p_{i-l,j-m,k-n}|}{p_{i,j,k}} > \beta_1 \quad l, m, n = 0, 1 \quad (11)$$

$$\max \left(\frac{|v_{i+l,j+m,k+n}^q - v_{i-l,j-m,k-n}^q|}{v_{i,j,k}^q} \right) > \beta_2 \quad l, m, n = 0, 1 \text{ and } q = x, y, z \quad (12)$$

$$\frac{|\rho_{b_{i+l,j+m,k+n}} - \rho_{b_{i-l,j-m,k-n}}|}{\rho_{b_{i,j,k}}} > \beta_3 \quad l, m, n = 0, 1 \quad (13)$$

where β_1, β_2 and β_3 are three parameters to be fixed. Let us comment the above criteria to identify a cell as a shocked one. As it is well known in 1D, across a shock, quantities such as p, v , and ρ have a jump discontinuity. The lack of numerical resolution may produce misleading results without a fine tuning of β parameters. For example, in the case of low values of β_1 , cells where there are only strong gradients could be identified as shocked cells. These problems can be extended to the other conditions. Some special attention deserves strong rarefactions. Since regions where the gas is being fast rarefied could satisfy the above conditions even with high values for β parameters, one new condition must be considered in order to avoid identifying strong rarefactions as shocks. This condition takes advantage from the fact that the velocity in the post-shock region is always greater than that of the pre-shock region (Colella & Woodward 1984), i.e.,

$$v_{i-1,j,k}^x > v_{i+1,j,k}^x \quad \text{or} \quad v_{i,j-1,k}^y > v_{i,j+1,k}^y \quad \text{or} \quad v_{i,j,k-1}^z > v_{i,j,k+1}^z \quad (14)$$

Some experimentation has been carried out so as to get the values for the parameters β_1, β_2 , and β_3 , and also to check their performance. As we have seen above, too low values for the parameters could be dangerous. However, high values could fail when the shocks present in the simulation were not too strong. In order to check conditions (11-14) we need a simulation involving shocks, contact discontinuities and rarefactions, based on a problem with a well known analytical solution. The results of a 3D analytical test presented by Quilis et al. (1996) have been used. The identification of the cells involved in the shock is excellent in this case. Although general results are more complex, the method seems to be

able to identify shocked cells reasonably. In the practical implementation presented in this paper, β parameters have been chosen under the constraints that the regions labelled in Fig. 6, as shock candidates, are most accurately recovered. The values used in this paper for those parameters, which fulfil the above criteria, are $\beta_1 = 3$, $\beta_2 = 2$, and $\beta_3 = 2$.

Collecting together all the previous prescriptions, Figure 7 shows some 3D plots of the shocked cells at several redshifts for A simulation. At high redshifts, the shocked cells form some sort of filaments which would be following the ones arising in DM (see Fig. 1). Then, we could say that these shocks, which appears at quite early times, come from the collapse of the substructure and from merging processes among these substructures. Between $z \sim 2$ and $z \sim 0$ the shocked cells mainly trace a quasi-spherical shock moving outwards from the cluster center. Morphologies of the shocks display filamentary structures at the early epochs – high redshift – while at lower redshift a quasi-spherical shock appears at the inner regions and propagates outwards dominating the global structure.

The presence of shocks is directly related with the dynamics of gas. By using the above conditions the number of shocked cells can be computed. Figure 8 plots the number of shocked cells versus time evolution for A(B) continuous(dashed) line. The maximum number of cells involved in shocks is at $z \sim 2$. This epoch is directly correlated with those times when the quasi-spherical shock in Figs. 3 and 4 starts to form.

3.3. Energy released by shocks

In previous section the presence of shocks has been discussed. Now we try to quantify the energy released by those shocks to ICM.

An easy way to quantify the shock heating is to compare some quantities obtained by the simulations with the values obtained considering an *analytical adiabatic evolution*. The

quantities derived from this analytical adiabatic evolution are labelled with tilde ($\tilde{}$). As it is well known in the adiabatic regime the pressure and temperature are related with density at any time in the following form:

$$\tilde{p} = \kappa \tilde{\rho}_b^{\tilde{\gamma}} \quad (15)$$

$$\tilde{T} = \eta \tilde{\rho}_b^{\tilde{\gamma}-1} \quad (16)$$

where κ and η are two constants. In order to fix the values of these constants we take the same values of pressure (p), density (ρ), and temperature (T) as the ones used, at the initial time, in the numerical simulations.

If the simulated cluster would evolve pure adiabatically, Eqs. (15-16) should give, at any time, the same values of pressure and temperature than those obtained from the hydro-code. In particular, if the baryonic density derived from the code were used as an input for the above adiabatic laws, and the cluster would evolve pure adiabatically, no differences should be found, at any time, between results from Eqs. (15-16) and the ones given by the numerical code. In practice, we compute all the pure adiabatic quantities ($\tilde{p}, \tilde{T}, \tilde{\rho}_b$) using as input the density coming from the simulations. Any deviations between results from the simulation A, and results from Eqs. (15-16) – where it has been used the density evolved by the A simulation – should be considered as a proof of the presence of non-adiabatic processes.

The total internal energy for the whole box is defined as :

$$E_U = \int_V \rho_b \epsilon dV \quad (17)$$

being V the physical volume.

Three total internal energies can be computed. First(second) is the one derived from the A(B) simulation. A third one is obtained from the analytical adiabatic evolution by using Eqs. (15-16). Top panel of Figure 9 shows total internal energy from A simulation

(continuous line) and B simulation (dashed-pointed line), and from analytical adiabatic evolution (dashed line). The curves from simulations appear clearly different from the analytical case. If the evolution were completely adiabatic, the internal energy for the A simulation (no cooling effects) should be identical to the one for the analytical adiabatic evolution. As this simulation does not consider cooling effects, all these differences are due to non-adiabatic processes. That means that shocks are the responsible of the most part of the ICM heating. The total internal energy for the B simulation is slightly lower than the one obtained in the A case at some phases of the evolution. These small differences are negligible in front of the differences between A or B cases against the analytical adiabatic evolution curve. Consequently, cooling effects are negligible compared with shocks.

Total kinetic energy is estimated from the following volume integral:

$$E_K = \frac{1}{2} \int_V \rho_b v^2 dV \quad (18)$$

Bottom panel of Figure 9 plots time evolution of the ratio E_U/E_K for the data generated by our simulations. Continuous (dashed-pointed) line corresponds to A(B) simulation. These curves show those times of the evolution where the internal energy is being released to the ICM by shocks. The decreasing branch in Figure 8, after the first maximum, is related with the epoch in which shocks – already formed – are propagating and losing energy, which contributes to the ICM heating. This branch is correlated with the raising branch of the E_U/E_K curve in Figure 9.

Figure 10 is a plot of the time evolution of the logarithm of the average temperature in a ball of one comoving Mpc radius centered at the core cluster. As usual, data generated by A (continuous line) and B (dashed-pointed line) simulations, and the analytical adiabatic evolution (dashed line) are displayed. As the observations suggest, the values of temperature obtained in our simulations range around $\sim 3 \times 10^7 K$ at low redshifts. Both simulations, A and B, show how the temperature has increased about six orders of magnitude over

that of the pure adiabatic evolution. There are no important differences between A and B temperatures, as in the case of the quantities analyzed previously.

Figure 11 plots – for the case B – the X-Ray thermal bremsstrahlung luminosity produced by a ball of one comoving Mpc radius centered at the core cluster. The values are compatible with those given by the X-Ray observations which range between 10^{42} and 10^{44} erg/s.

4. Discussion

In this paper we have used some numerical techniques recently applied to Cosmology. These techniques, HRSC, seems to be the most suitable in order to study the role of shocks in galaxy cluster evolution. The choice is justified by their properties to handle shocks. The capability of these techniques to capture shocks with very small diffusion is independent of the resolution used in the numerical simulations. Hence, by construction, shocks are captured even using coarse grids. This property is crucial in 3D applications.

Previous sections illustrate the fact that non adiabatic processes, due to shocks, take an important role in the description of the ICM. In the model presented in this paper, that is, a baryonic fluid plus dark matter component coupled gravitationally, shocks are able to heat the ICM until values compatible with observational data.

The calculations have been carried out in two cases: with and without cooling processes. This procedure allows us to distinguish between non-adiabatic effects coming from shocks and the ones from cooling. The role of the cooling, even when it could be important in other scenarios, is irrelevant for the simulations considered in this paper, while shocks play the most important role.

In the picture describing the dynamics of the baryonic component, there are some clues

showing the presence of shocks. Examining the quantities sensitive to shocks, all of them evidence the formation of a quasi-spherical shock. This shock seems to arise around $z \sim 2$ at the cluster center and moves outwards. Nevertheless, some irregular shocks could form at $z \geq 2$. This conclusion is supported by the behaviour of the entropy profiles (see Fig. 5), and the existence of shocked cells at these times (see Fig. 8). The quasi-spherical shock would form from the collapse of the quasi-spherical global structure, while other smaller shocks – with a filamentary morphology – would arise from some collapsing substructure and merging processes. In short, previous discussion manifest two different regimes in the shock formation.

It should be noticed that the structures simulated in this paper correspond, due to the initial conditions, to a large Abell cluster. For this kind of clusters, gravitational collapse is fast and the dynamics is violent. Shocks form earlier and are stronger than in others smaller cluster-like objects ($< 3\sigma$).

Some discussion on the numerical resolution of the simulations is needed. The one used in present paper ($\sim 0.3Mpc$) is not enough to simulate the very center of the clusters and galaxy formation, but it suffices to study the role of the shocks in ICM. It should be kept in mind that HRSC techniques are able to resolve shocks even with coarse grids. Nevertheless, higher resolution would be desirable to perform more complete simulations. Improvements in numerical resolution will introduce smaller scales in the problem, as a consequence, the physics of the model should be enriched in order to describe this new scenario. Chemical reactions and radiative transfer should be considered.

This work has been supported by the Spanish DGES (grants PB96-0797 and PB94-0973). V. Quilis thanks to the Conselleria d’Educació i Ciència de la Generalitat Valenciana for a fellowship. Dr. P. Anninos and Dr. J.M^a. Martí are acknowledged for useful discussions. One of the authors, V.Q., thanks Dr. S.M.D. White for the hospitality

during his visit to *Max-Planck-Institut für Astrophysik*. Authors gratefully acknowledge the enlightening comments of the referee. Calculations were carried out in a HP J280 and in two SGI Origin 2000, at the *Centre Europeu de Paral·lelisme de Barcelona (CEPBA)* and the *Centre de Informàtica de la Universitat de València*.

A. Energy conservation properties

As it is well known, in simulations without cooling the total energy must be conserved. This conservation law can be obtained after integrating on the whole computational volume the evolution equations, and it reads as follows (Peebles 1980):

$$\frac{d(\tilde{E} + W)}{dt} + \frac{\dot{a}}{a}(2\tilde{E} + W) = 0 \quad (\text{A1})$$

where \tilde{E} is the total energy – kinetic of the gas plus kinetic of the particles plus internal for the gas– and W is the total gravitational energy, i.e., gas plus particles.

The Eq.(A1) can be integrated respect to the scale factor giving:

$$a(t_2)\tilde{E}(t_2) - a(t_1)\tilde{E}(t_1) + \int_{a(t_1)}^{a(t_2)} \tilde{E}da = -(a(t_2)W(t_2)) - a(t_1)W(t_1) \quad (\text{A2})$$

being t_2 and t_1 two different times. The energy conservation can be tested by defining a quantity, R , as:

$$R(t) = \frac{a(t)\tilde{E}(t) - a(t_1)\tilde{E}(t_1) + \int_{a(t_1)}^{a(t)} \tilde{E}da}{-(a(t)W(t)) - a(t_1)W(t_1)} \quad (\text{A3})$$

Consequently with Eq. (A2), quantity R must remain equal to unit during the evolution.

We have tested the energy conservation for the whole code , i.e., hydrodynamical and particle codes, coupled through the multidimensional Poisson solver. One numerical simulation with the same initial condition as in the case A, and with 64^3 cells and 64^3 particles has been considered. Figure 12 plots the quantity R against redshift. The maxima

errors are around three per cent. As it is well known, the better resolution (finer grids and more particles), the better conservation properties.

B. Some comments on the resolution of the hydrodynamical code

Due to the coarse grids we have used in this paper, our results depend strongly on the spatial resolution. Our numerical simulations have been performed using the hydro-code described in Quilis et al. (1996). In that paper the authors discussed two types of reconstruction procedures as methods to increase the spatial resolution of the algorithm, i.e. MUSCL (linear) and PPM (parabolic). In order to investigate the influence of the numerical resolution in our galaxy cluster simulations, we have considered some numerical experiments. In order to do that, some simulations without cooling and with the same initial conditions than in A case (see Section 2) have been performed.

The above two reconstruction procedures have been considered. Together with the reconstruction, we have studied the influence of the number of cells and particles used in the simulations. Extremely coarse grids with 64^3 cells and 64^3 particles, and the one used in the simulations in this paper, 128^3 cells and 128^3 particles, have been considered.

Table 1 summarizes the main results of these experiments. We show the maxima of the density contrast of the gas, δ_b^{max} , at two times. At each time, these maxima are presented for both grids and set of particles, i.e. 64^3 and 128^3 , and for MUSCL and PPM reconstructions. As it follows from that table, with the grids considered, MUSCL does not work properly. PPM appears as the best procedure to increase the spatial resolution, in this sense, the simulations presented in this paper have been computed using PPM reconstruction procedure.

Table 1: Influence of the numerical resolution.

	z	MUSCL64	PPM64	MUSCL128	PPM128
δ_b^{max}	1	24.5	56.3	53.2	210.5
δ_b^{max}	0	11.5	96.0	31.5	348.8

REFERENCES

- Anninos, P., Norman, M.L. & Clarke, D.A. 1994, *ApJ*, 436, 11
- Anninos, P. & Norman, M.L. 1996, *ApJ*, 459, 12
- Bertschinger, E. & Gelb, J.M. 1991, *Computer in Physics*, 5, 164
- Bryan, G.L., Cen, R., Norman, M.L., Ostriker, J.P. & Stone, J.M. 1994, *ApJ*, 428, 405
- Cen, R. 1992, *ApJS*, 78, 341
- Colella, P. & Woodward, P.R. 1984, *J. Comp. Phys.*, 54, 174
- Einfeldt, B., Munz, C.D., Roe, P.L. & Sjögren, B. 1991, *J. Comp. Phys.*, 92, 273
- Evrard, A.E. 1988, *MNRAS*, 235, 911
- Efstathiou, G., Davis, M., Frenk, C.S. & White, S.M.D. 1985, *ApJS*, 57, 241
- Gingold, R.A. & Monaghan, J.J. 1977, *MNRAS*, 181, 375
- Gnedin, N.Y. 1995, *ApJS*, 97, 231
- Godunov, S.K. 1959, *Matematicheskii Sbornik*, 47, 271
- Guzzo, L. 1996, in *ASP Conference Series 94, Mapping, Measuring, and Modelling the Universe*, ed. Coles, P., Martinez, V.J., and Pons-Borderia M.J. (San Francisco, Astronomical Society of the Pacific) 157
- Harten, A. 1983, *J. Comp. Phys.*, 49, 357
- Hernquist, L. & Katz, N. 1989, *ApJS*, 64, 715
- Hockney, R.W. & Eastwood, J.W. 1988, *Computer simulation using particles*. IOP Publishing

- Hoffman, Y. & Ribak, E. 1991, ApJ, 380, L5
- Kang, H., Ostriker, J.P., Cen, R., Ryu, D., Hernquist, L., Evrard, A.E., Bryan, G.L. & Norman, M.L. 1994, ApJ, 430, 83
- Lucy, L.B. 1997, AJ, 82, 1013
- Navarro, J.F. & White, S.D.M. 1993, MNRAS, 265, 271
- Navarro, J.F., Frenk, C.S. & White, S.D.M. 1995, MNRAS, 275, 720
- Peebles, P.J.E. 1980, The Large-Scale Structure of the Universe (Princeton: Princeton Univ. Press)
- Press, H., Flannery, B.P., Teukolsky, S.A. & Vetterling, W.T., 1987, Numerical Recipes. The art of Scientific Computing. Cambridge University Press
- Quilis, V., Ibáñez, J.M^a. & Sáez, D. 1996, ApJ, 469, 11
- Roe, P.L. 1981, J. Comp. Phys., 43, 357
- Ryu, D., Ostriker, J.P., Kang, H. & Cen, R. 1993, 414, 1
- Tsai, J.C., Katz, N. & Bertschinger, E. 1994, 423, 553
- Umemura, M. & Ikeuchi, S. 1984, Prog. Theor. Phys. 72,47
- van den Weygaert, R. & Bertschinger, E. 1996, MNRAS, 281, 84
- Xu, G. 1995, ApJS, 98, 355

Fig. 1.— Dark matter particles distribution inside the computational boxes for six epochs for A simulation. Boxes are 20 comoving Mpc length per edge. Only 32^3 particles are displayed in each box.

Fig. 2.— Slices along z-axis of the gas density contrast for A simulation. Each slice is 20 comoving Mpc length per edge and 0.15 comoving Mpc depth. Columns stand for fixed redshift. Central rows are centered at the maximum density contrast, up(low) row is located at -5(+5) comoving Mpc from the central slices along z-axis. At left side of each slice there is one palette describing the colour scale used to plot it.

Fig. 3.— Average density contrast, for A simulation, in radial shells for gas(top) and DM(bottom). Six times are displayed. Radii are in comoving Mpc.

Fig. 4.— Average radial velocities, for A simulations, in radial shells for gas(top) and DM(bottom). Six times are displayed. Radii are in comoving Mpc and velocities in units of speed of light (c).

Fig. 5.— Average entropy in radial shells for gas in A simulations. Six times are displayed. Radii are in comoving Mpc. Entropy is defined as $s = \ln(T/\rho_b^{\gamma-1})$.

Fig. 6.— From top to bottom, slices show (for the baryonic component): divergence of velocity in units of c (first row), entropy (second row), temperature in K (third row), and pressure in dyn/cm^2 (fourth row). Each slice is 20 comoving Mpc length per edge and 0.15 comoving Mpc depth. Columns stand for a fixed redshift. All slices are centered at the maxima of the density contrast. At left side of each slice there is one palette describing the colour scale. Results correspond to A simulation.

Fig. 7.— Shocked cells inside the computational boxes for six times for A simulation. Boxes are 20 comoving Mpc length per edge.

Fig. 8.— Number of shocked cells (N_{shc}) versus redshift. Continuous(dashed) line plots A(B) simulation.

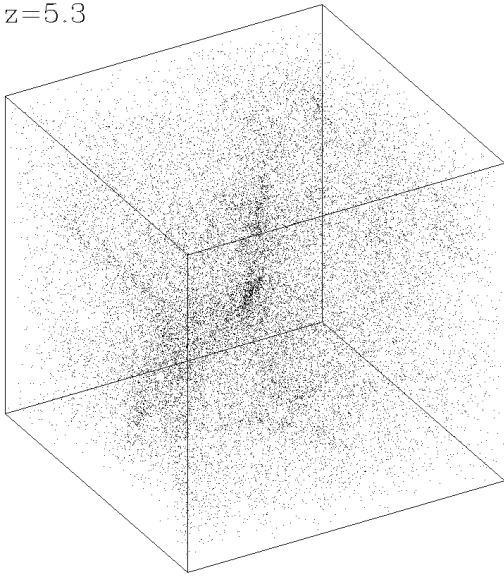
Fig. 9.— Plot of logarithm of the total internal energy (E_U) against redshift (top panel) and the ratio of the total internal energy (E_U) to the total kinetic (E_K) energy versus redshift (bottom panel). All energies are in units of ergs. Continuous (dashed-pointed) line stands for A(B) results, in top panel dashed line shows analytical adiabatic result.

Fig. 10.— Plot of the logarithm of the average temperature (in K degrees) in a ball of 1 comoving Mpc centered at the core cluster. Continuous, dashed-pointed, dashed lines stands for A and B simulations, and analytical adiabatic evolution, respectively.

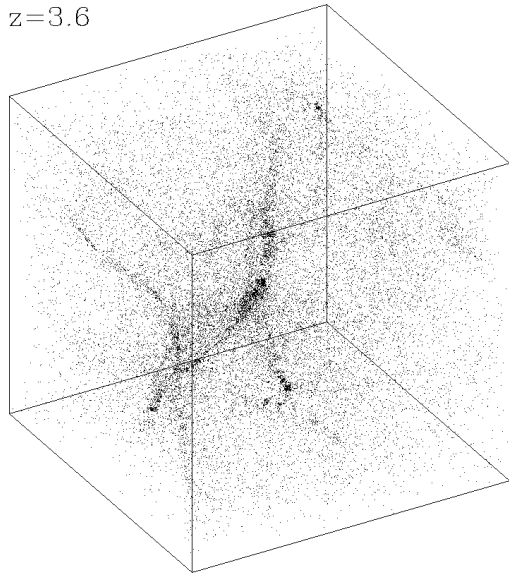
Fig. 11.— Plot for B simulation of the logarithm of the X-Ray luminosity (in erg/s), from a ball of 1 comoving Mpc, centered at the core cluster.

Fig. 12.— Plot for the quantity R defined in Eq. (A3) against the redshift. Perfect energy conservation would imply $R = 1$.

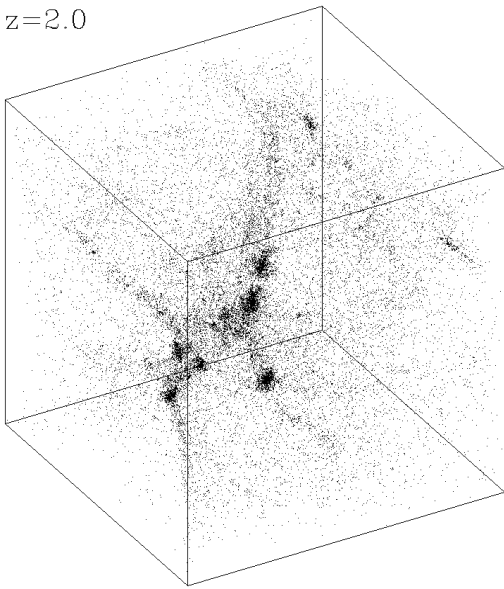
$z=5.3$



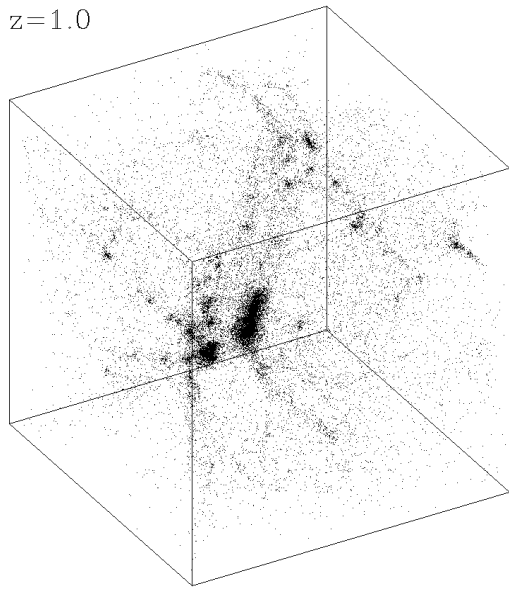
$z=3.6$



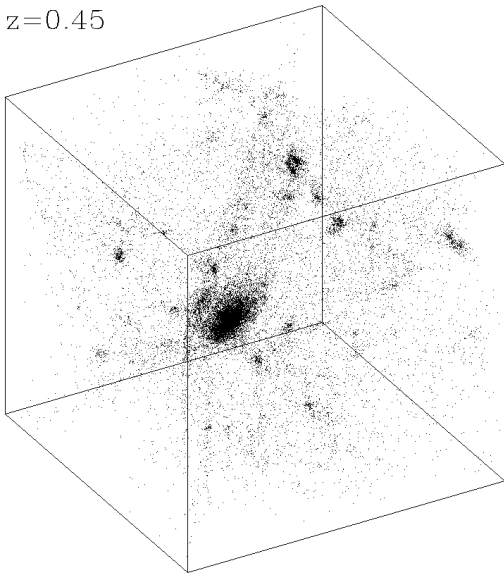
$z=2.0$



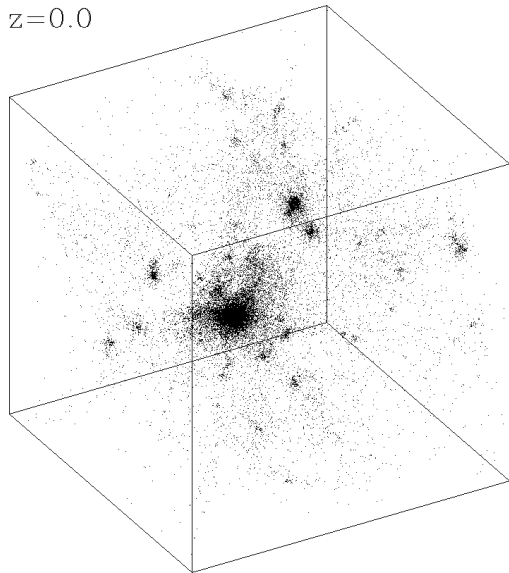
$z=1.0$

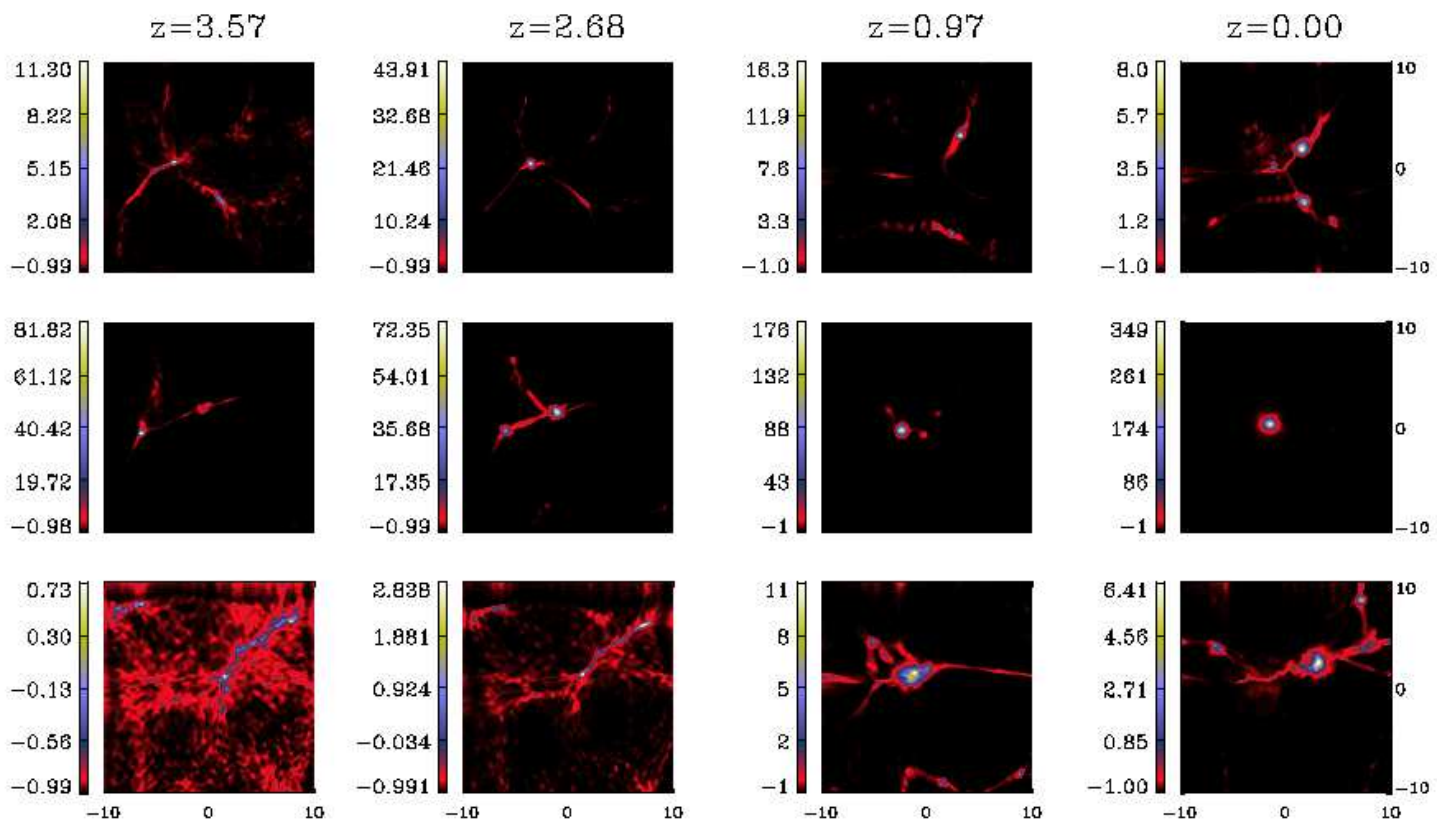


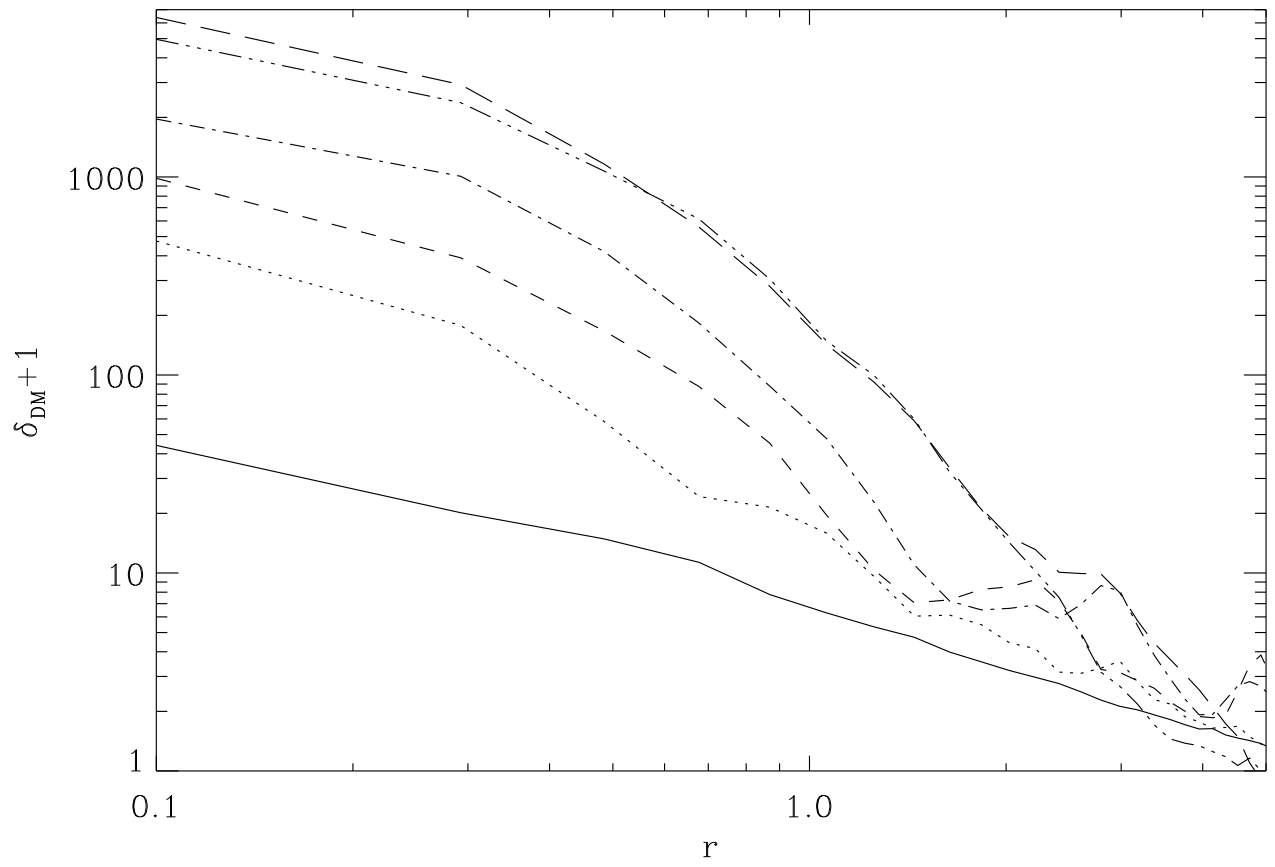
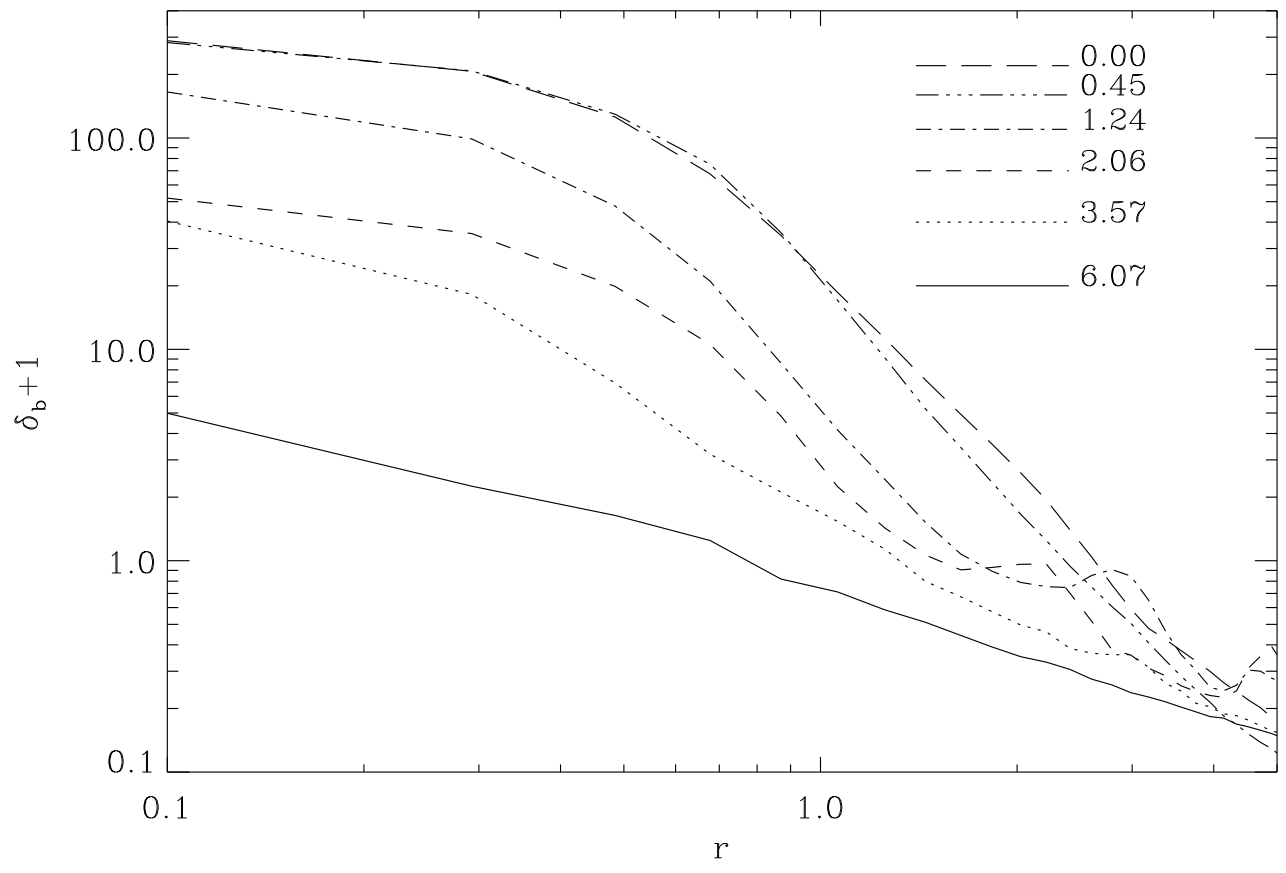
$z=0.45$

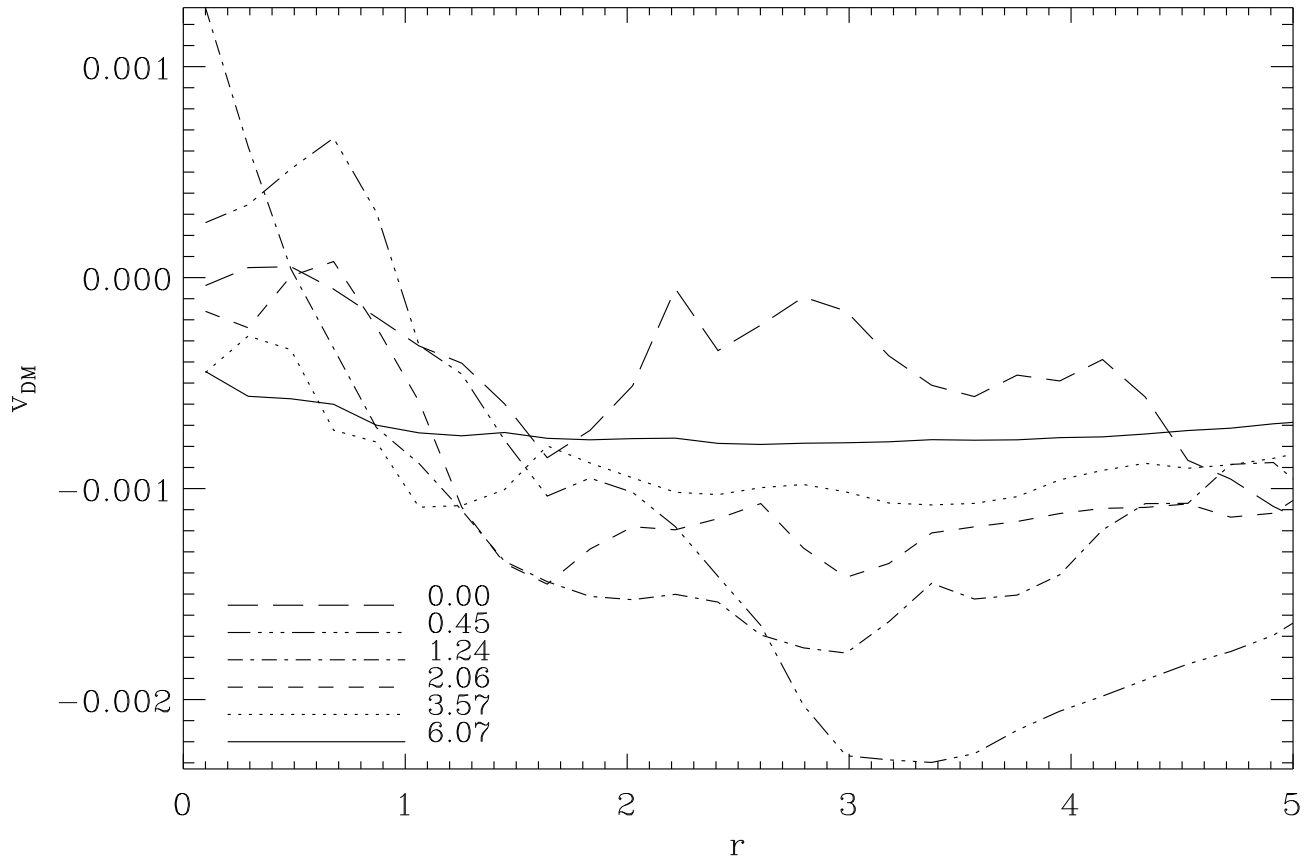
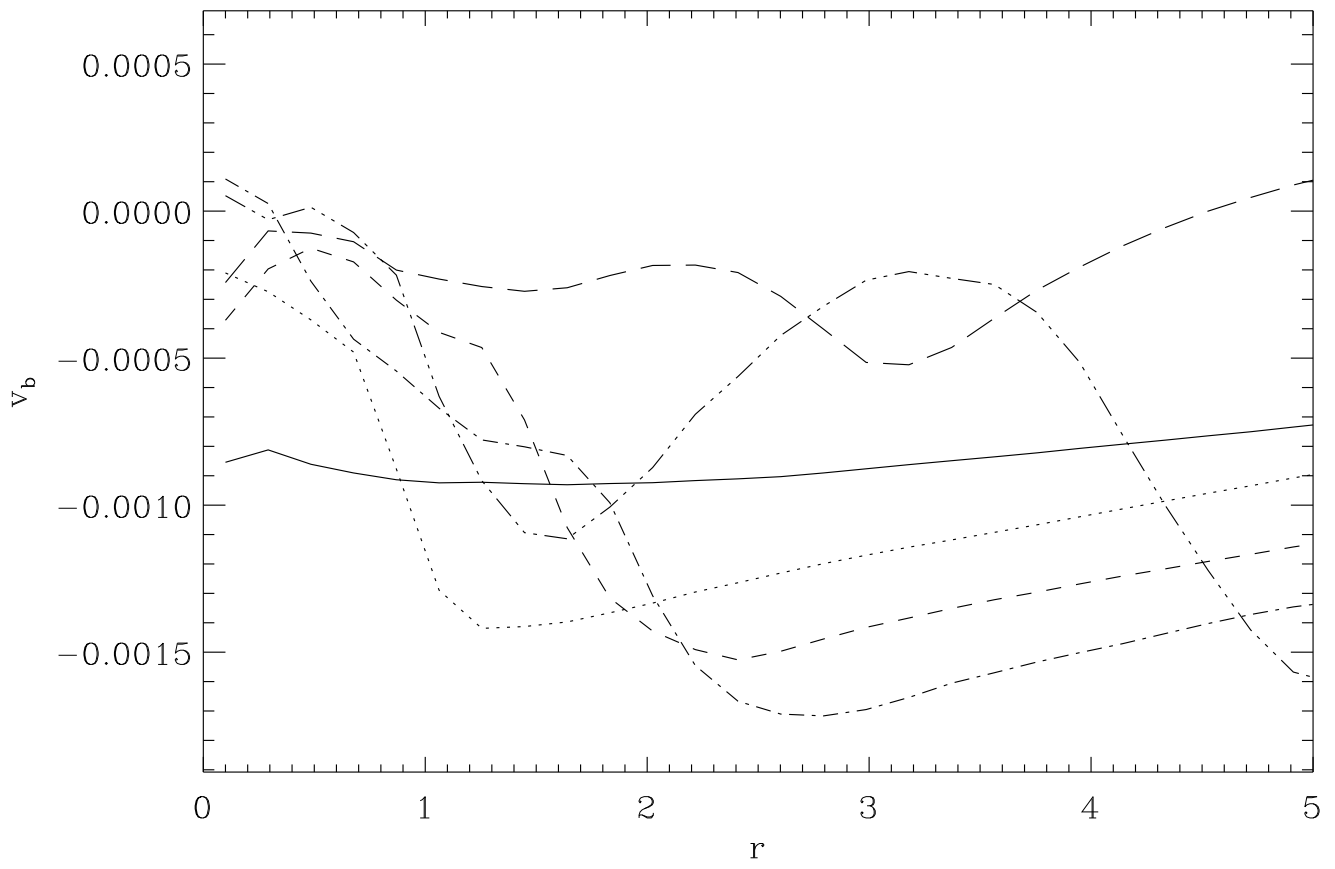


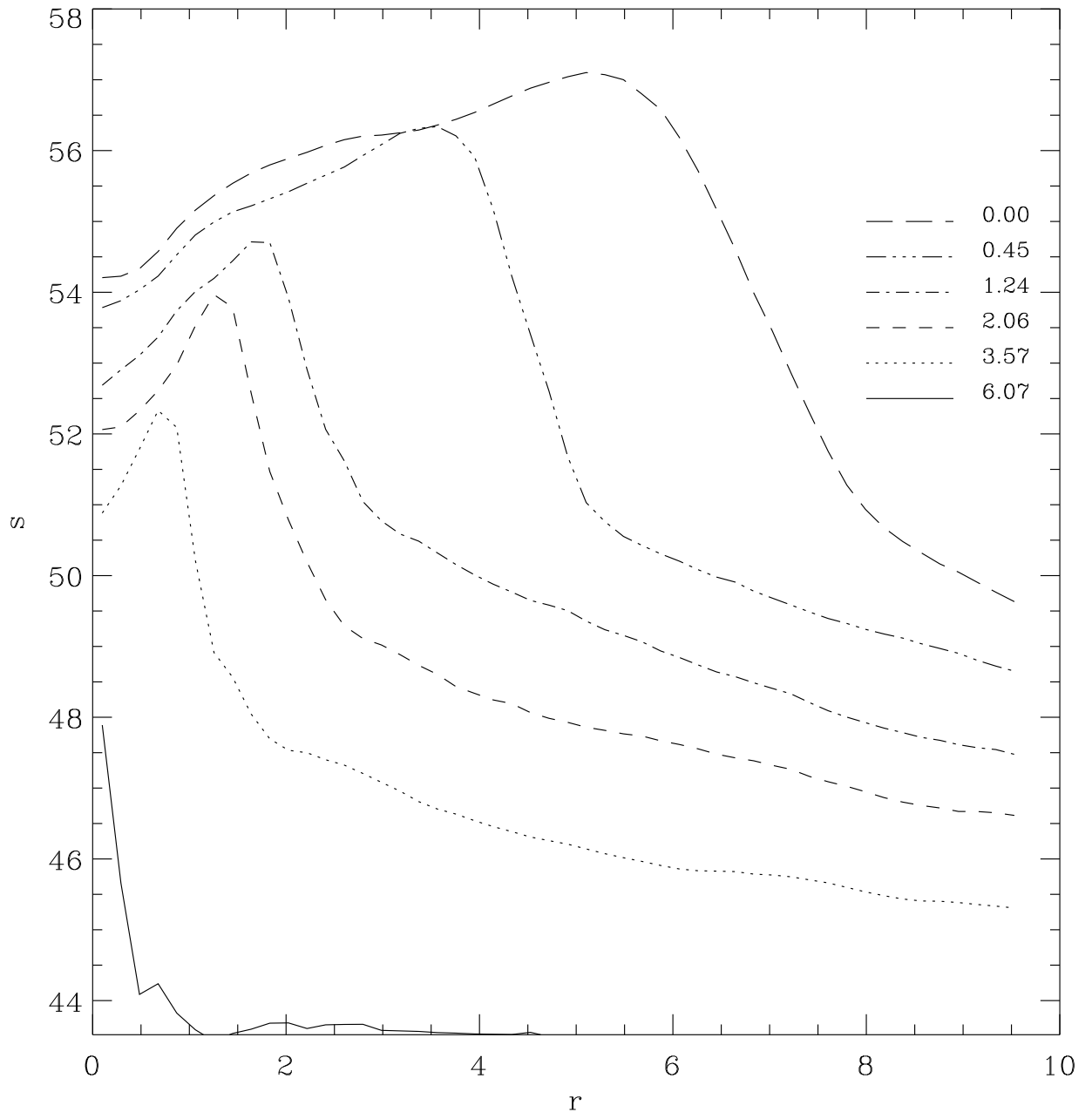
$z=0.0$

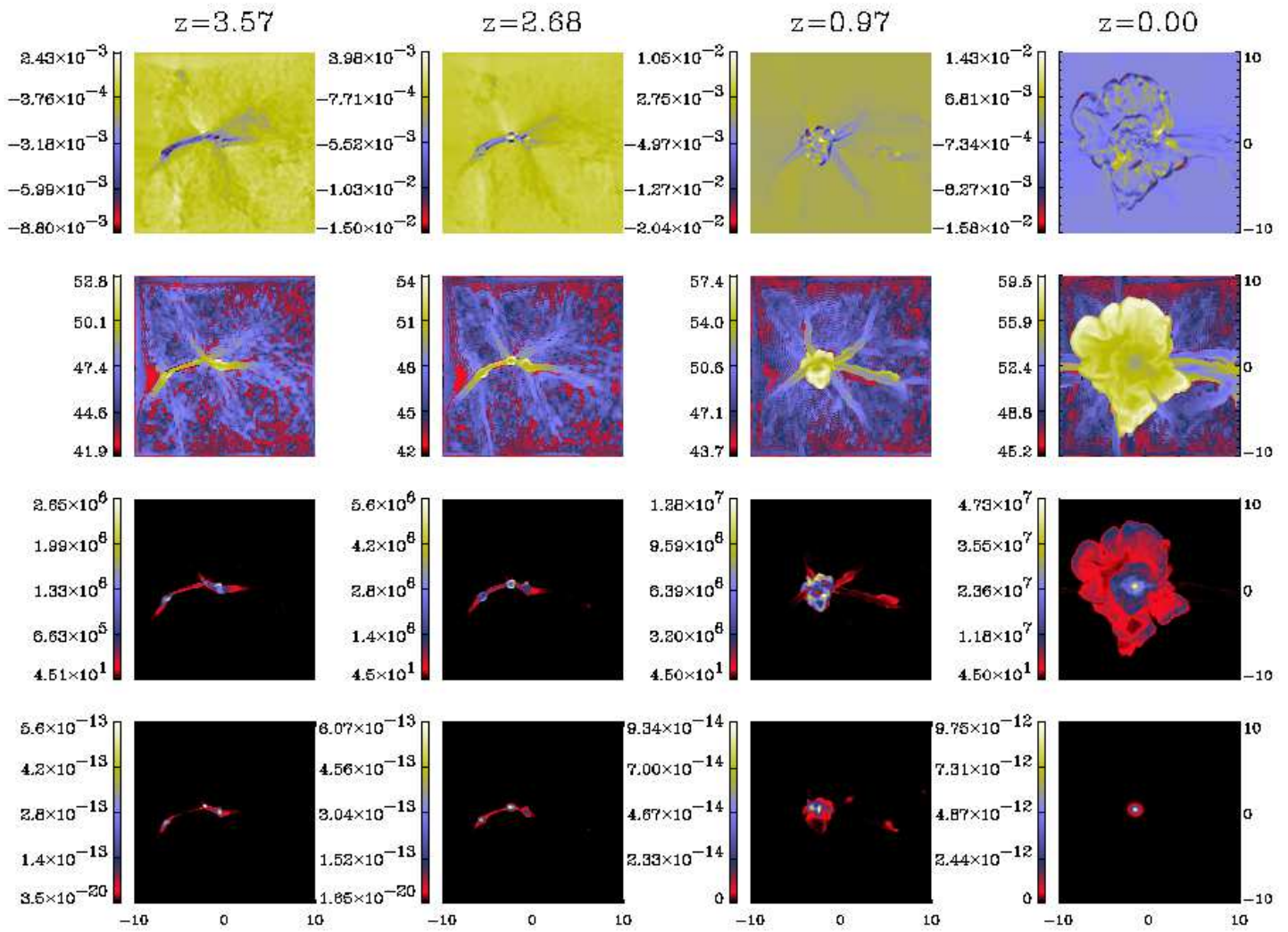




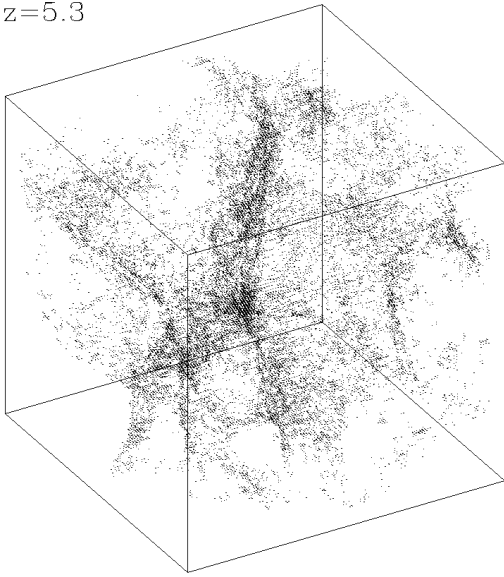




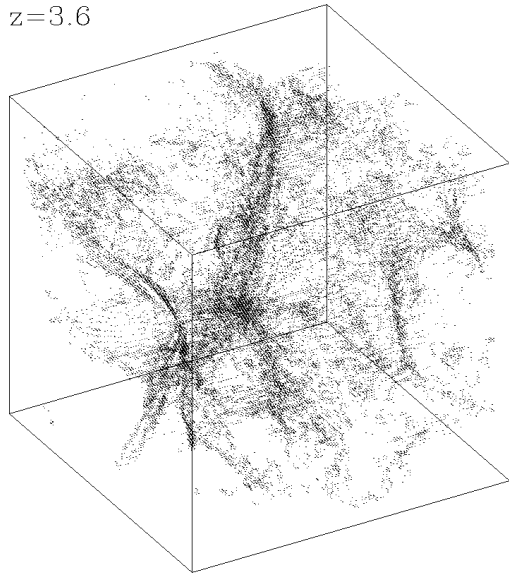




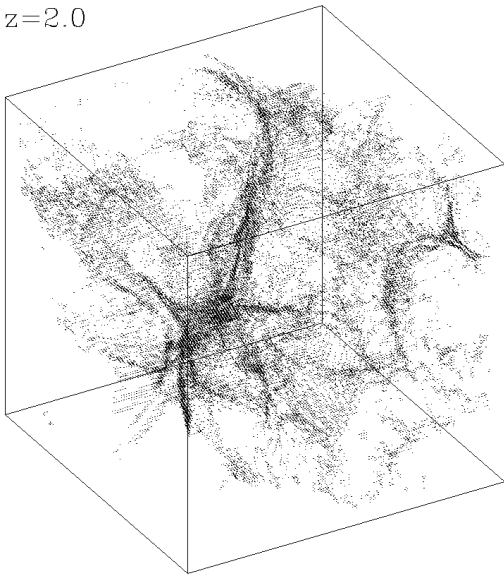
$z=5.3$



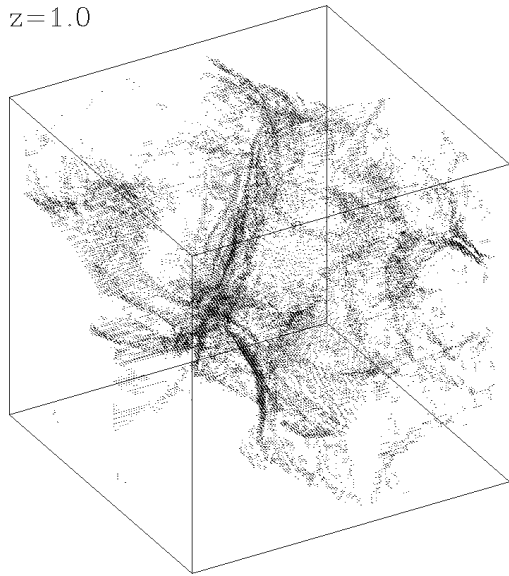
$z=3.6$



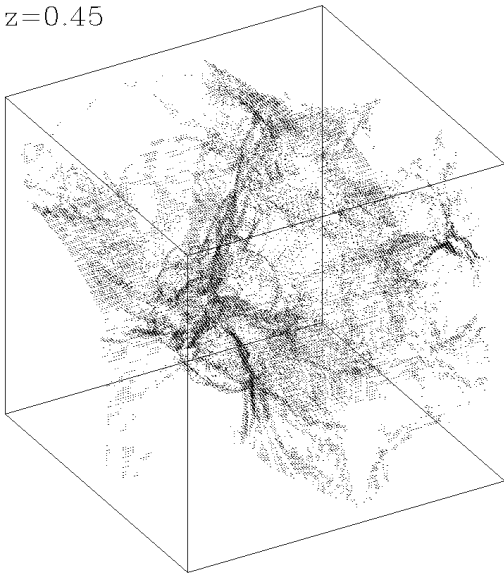
$z=2.0$



$z=1.0$



$z=0.45$



$z=0.0$

